Geomechanics and Engineering, *Vol. 23, No. 6 (2020) 503-512*
DOI: https://doi.org/10.12989/gae.2020.23.6.503

Thermographic analysis of failure for different rock types under uniaxial loading

Alper Kırmacı* and Mustafa Erkayaoğlu[a]

Department of Mining Engineering, Middle East Technical University,
Üniversiteler Mahallesi, Dumlupınar Bulvarı No.1, 06800 Çankaya/Ankara, Turkey

(Received February 4, 2020, Revised December 5, 2020, Accepted December 9, 2020)

Abstract. Mining activities focus on the production of mineral resources for energy generation and raw material requirements worldwide and it is a known fact that shallow reserves become scarce. For this reason, exploration of new resources proceeds consistently to meet the increasing energy and raw material demand of industrial activities. Rock mechanics has a vital role in underground mining and surface mining. Devices and instruments used in laboratory testing to determine rock mechanics related parameters might have limited sensing capability of the failure behavior. However, methodologies such as, thermal cameras, digital speckle correlation method and acoustic emission might enable to investigate the initial crack formation in detail. Regarding this, in this study, thermographic analysis was performed to analyze the failure behaviors of different types of rock specimens during uniaxial compressive strength experiments. The energy dissipation profiles of different types of rocks were characterized by the temperature difference recorded with an infrared thermal camera during experiments. The temperature increase at the failure moment was detected as 4.45°C and 9.58°C for andesite and gneiss-schist specimens, respectively. Higher temperature increase was observed with respect to higher UCS value. Besides, a temperature decreases of about 0.5-0.6°C was recorded during the experiments of the marble specimens. The temperature change on the specimen is related to release of radiation energy. As a result of the porosity tests, it was observed that increase in the porosity rate from 5.65% to 20.97% can be associated to higher radiation energy released, from 12.68 kJ to 297.18 kJ.

Keywords: failure; laboratory analysis; rock; stress-strain relations; energy geomechanics

1. Introduction

Rock mechanics is a field of research that analyses the behavior of rocks under stress and tension conditions. It has an essential role in tunneling activities, underground and surface mining. It is commonly the basis of engineering studies, such as the design of underground openings, bench stability, tunneling activities, dam construction, or storing nuclear waste in rock settings (Deb and Verma, 2006). Theoretical studies of rock mechanics started at the beginning of the 1900s (Ulusay *et al.* 2016) and it is known that there are still points that could be improved related to the integration of new technologies both on laboratory scale and in field studies. For example, researchers currently investigate the behavior of crack and failure with the help of available technologies such as high-speed cameras (He *et al.* 2015, Zhang and Zhao 2014), thermal infrared cameras, digital speckle correlation method (Jin *et al.* 2003, Hong-lin 2013, Ma *et al.* 2004, Ma *et al.* 2006) and acoustic emission systems (Kong *et al.* 2018, Aydan and Ulusay 2013, Read 2004, Young and Collins 2001). Researchers in this field commonly focused on the determination of the temperature change at the failure moment (Lou and He 2018, Antony *et al.* 2017, Pappalardo *et al.* 2016, Wang *et al.* 2016, Aydan *et al.* 2014, Tan *et al.* 2007, Liu *et al.* 2006, Wu *et al.* 2006).

The temperature changes during the experiments cause energy losses in the form of dissipation because of the formation and coalescence of cracks. As a result of the deformation of rock samples, energy is released in different forms, such as elastic energy, plastic energy, and kinetic energy (Xie *et al.* 2009). Salami *et al.* (2017) stated that quantifying the heat generation will lead to a better understanding of energy dissipation on rocks and concluded that the most significant part of the plastic energy is dissipated as heat from the rock specimen. This supports the concept of temperature measurement during rock mechanics experiments to investigate the energy released from the rock specimen. Since porosity rate can affect the structure of the rock, it also plays an essential role for the characterization of rocks (Tan *et al.* 2016, Lee *et al.* 2016, Go *et al.* 2014).

The total amount of released energy from a rock specimen can theoretically be estimated from the stress vs. axial deformation graphs. This interpretation can be affected by the structural changes in the samples (Gui *et al.* 2016) and the temperature change in the rock sample has an essential role on the failure behavior. According to Pasten *et al.* (2015) and Yin *et al.* (2015), failure behavior and experiment results might vary after the rock samples are exposed to elevated temperatures. Similarly, Yin *et al.* (2018), Chen *et al.* (2017) and Abuel-Naga *et al.* (2013)

*Corresponding author, Ph.D. Student
E-mail: kirmaci@metu.edu.tr
[a]Assistant Professor
E-mail: emustafa@metu.edu.tr

ISSN: 2005-307X (Print), 2092-6219 (Online)

Fig. 1 MTS 815 test system with COX thermal camera

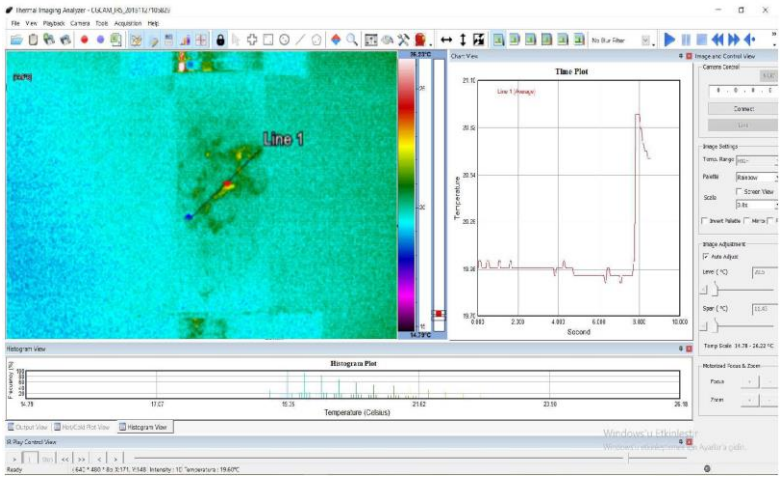

Fig. 2 Interface of the thermal camera software

stated that different temperature profiles acting on liners that cover rock material underground, affects the behavior of the liners. For these reasons, the thermographic analysis with the help of the thermal cameras can provide more detailed information about the failure behaviors of rocks and the safe production conditions of the working area, especially in underground environment.

This study aims to introduce reliable and accurate data of thermographic analysis of rock samples with the help of a longwave thermal camera. The failure behavior of rock samples and the energy generated during the uniaxial compressive strength (UCS) test are investigated for different type of rocks. In this way, inferences about the results of the experiments can be supported by thermographic data aiming to overcome the limitation of visual interpretation of rock mechanics tests. Most of the studies in the literature were carried out with the help of mid-wave high speed thermal cameras and in this study, the applicability of thermographic analysis with a longwave thermal camera was investigated.

2. Methodology and experimental setup

The methodology of this study covers the laboratory tests of different types of rocks as andesite, gneiss-schist, and marble. UCS tests were conducted to monitor the failure behavior of rock specimens with a longwave infrared thermal camera. The camera was placed in front of the experimental setup to monitor the failure behavior from a distance of about 1 m. The temperature changes were monitored in real-time by the software of the thermal camera during the experiments and recorded for further analysis. Different loading cycles were defined in the MTS 815 device which is a displacement-controlled testing environment with a maximum loading capacity of up to 500 kN. Fig. 1 shows the MTS testing system together with the thermal camera setup.

The experiments were recorded by a thermal camera manufactured by COX as seen in Fig. 1. The camera is an uncooled long-wavelength infrared thermal camera with update period of 0.03 seconds in full fps settings. The wavelength range visible to the human eye is between 400 and 700 nanometers, whereas the infrared range is between 750 nanometers and 1-millimeter wavelength. Therefore, the infrared rays cannot be seen by human eye. Thermal cameras can convert these infrared rays to visible images. For this reason, using a thermal camera instead of a video camera in the analysis of the experimental results might provide more detailed information about the behavior of the

Table 1 General information about the UCS experiments

Rock Type	Sample Diameter (mm)	Sample Length (mm)	Number of Experiments
Andesite	75	175	5
	63	145	14
	53	120	5
	42	100	5
Marble	75	175	5
	63	145	9
	53	120	5
	42	100	5
Gneiss-Schist	63	145	25

rock sample during failure.

According to Vollmer and Möllmann (2017), long-wavelength thermal cameras operate at 8-14×10^{-6} m, medium-wavelength thermal cameras at 3-5×10^{-6} m, and short-wavelength thermal cameras operate at the wavelengths up to 1.5×10^{-6} m. At room temperature, the wavelength emitted from the objects is at a maximum level of 10×10^{-6} m. At 300°C, the emitted wavelength is 5×10^{-6} m and as a comparison the emitted wavelength from the sun is 0.5×10^{-6} m. For these reasons, it was considered that a suitable type of camera for the laboratory experiments was the long-wavelength thermal camera. An uncooled thermal camera was used for this study based on the scope of the research and the requirement of continuous maintenance related to additional components of the cooling system. Besides, cooling systems are often used for long-distance measurements. The uncooled systems are more commonly used with long-wavelength cameras while the cooling systems can be used with medium and short-wavelength cameras.

The software of the thermal camera used to analyze the results enables the user to divide the displayed area per pixel dimensions, providing the temperature value recorded at the center of each pixel. Profiles in shapes such as square, rectangle, or circle can be defined on any desired region via the interface of the software to query the temperature readings. In this area, average, minimum, and maximum temperature values can be determined. The real-time graphs of the recorded temperature values can also be plotted on the interface of the software as given in Fig. 2.

Thermal cameras divide recorded images into pixels based on their resolution, which improves the image quality in direct proportion to the number of pixels. The camera used in the experiments has a resolution of 640x480 dividing the image into 307,200 squares with 640 pixels from the left and 480 pixels from the top. The defined profiles on any region, for example the line profile as seen in Fig. 2, enables to select through a region of pixels after the experiment is completed to analyze temperature changes in detail. This way, the results of the experiments can be interpreted specifically in the failure regions and the coordinates of this region can be obtained. A standard evaluation procedure was followed throughout the experiments where the values were monitored from the beginning of the experiments until the moment of failure including a predetermined period of post-failure. As a result, the temperature change occurring in the failure zone could be followed in detail during the UCS tests.

By following the ISRM suggested methods in terms of the ratio between sample length and diameter, UCS tests were performed in accordance with the recommended specimen geometries. Different diameters for andesite, marble, and gneiss- schist samples were used for the UCS tests. Table 1 summarizes the number of the performed UCS experiments within the scope of this study.

Andesite and marble samples were prepared with different diameters of 75 mm, 63 mm, 53 mm, and 42 mm diameter. The number of experiments conducted on andesite and marble specimens with 63 mm diameter were increased as the comparison of temperature increase was based on the available gneiss-schist specimens that were prepared from drill cores of the same diameter. As it was discussed, rocks release energy in different forms during their deformation. The total amount of energy can theoretically be found by the area under the stress-strain graphs. With the help of the thermal camera, it was possible to monitor the temperature difference during the experiment and specifically at the moment of failure. By using these values, the amount of energy related to radiation can be found from the Eqs. (1) and (2). The thermal exchange rate can be found with the help of the following equations;

$$Thermal\ \ Exchange\ \ Rate = k \times \frac{A}{h} \times (\Delta T) \quad (1)$$

$$Radiation\ \ Energy = Thermal\ \ Exchange\ \ Rate \times (\Delta t) \quad (2)$$

In these equations, k represents the thermal conductivity coefficient, A is the surface area of the sample, h represents the height of the sample, ΔT is the temperature change, and Δt represents the elapsed time during the experiments. The proportion of radiation energy released by rock material based on the total energy can be estimated by using experiment results. Different types of rocks were used in the experiments, and the thermal conductivity coefficients for each of these rocks are different and are determined as 3.20 for andesite, 3.00 for marble, 3.24 for gneiss, and 3.14 for schist type of rocks (Cermak and Ryback 1982).

3. Experimental results

The experiments were performed on samples prepared with different diameters and by using constant displacement rate of 0.002 mm/s. As a result of the experiments conducted on andesite samples, temperature increase was observed at the failure moment for most of the cases. Although all experiments were completed according to the same procedure, some experiments could not be monitored effectively by the thermal camera. There are several reasons of these non-valid tests by means of thermographic analysis. Firstly, there is no systematic way of predicting the failure behavior unless the specimens are prepared with designed notch geometries and angles. The failure of the

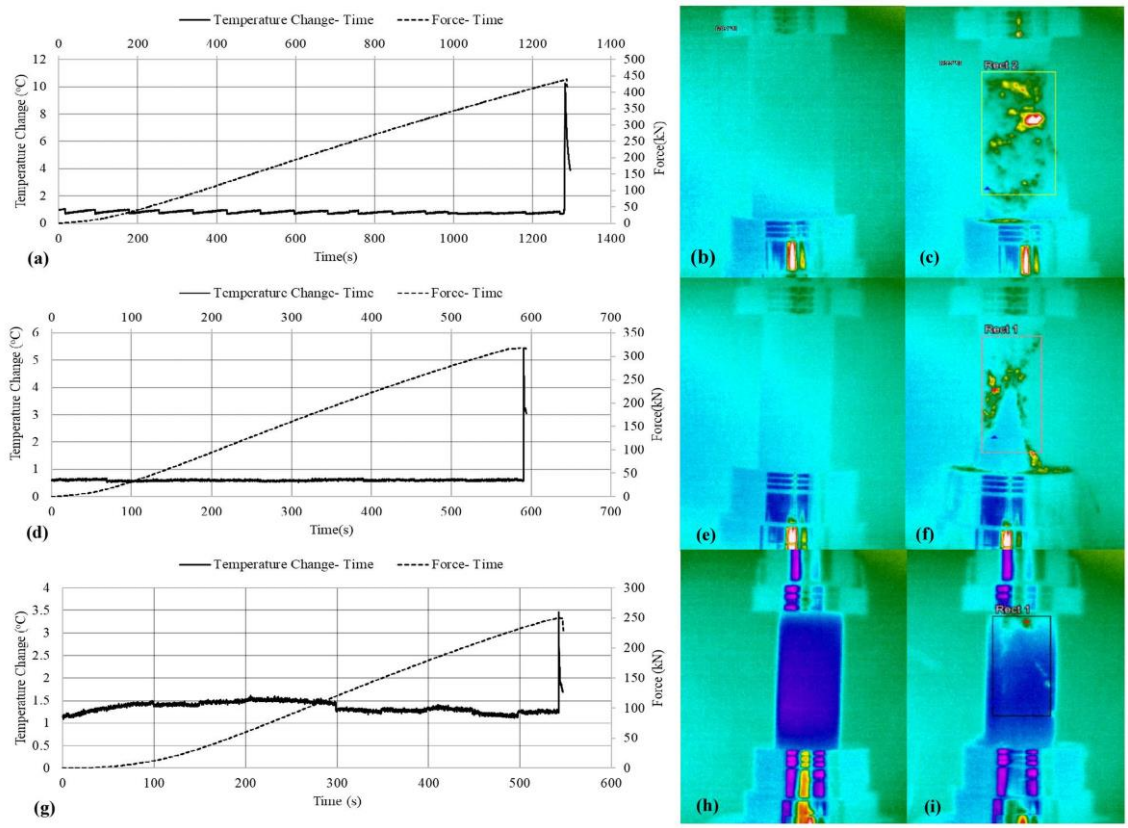

Fig. 3 (a), (d), (g) Temperature change- failure load- time graph of andesite samples, (b), (e), (h) Thermography image of andesite samples before failure and (c), (f), (i) Thermography image of andesite samples after failure

Table 2 Average results of different size of andesite samples

Sample Diameter (mm)	Failure Load (kN)	Temperature Increase (°C)	Radiation Energy (kJ)
75	437.60	10.29	297.18
63	283.29	4.45	139.21
Average	334.73	6.40	191.87

rock specimen can be initiated internally which means that it might not be detected from the surface of the sample until a visible crack is formed. Another drawback was that the thermal camera could not detect some of the failure cases that first occurred on the opposite side of the sample where the camera was not located. The main challenge is the temperature increase occurring in the sample as a sudden event and the thermal camera not being able to capture this moment for same cases. Therefore, the temperature increase obtained as a result of some experiments were considered to be non-valid due to the low level of energy released. Maximum temperature values recorded during tests were used for evaluation of all experimental results. Fig. 3 shows the graphs at the failure moments for andesite samples of valid experiments for which a significant temperature increase was observed. Although andesite specimens with different diameters were prepared for the UCS tests, only samples with 75 mm and 63 mm resulted in a significant temperature increase at the failure moment. Fig. 3(a)-3(c) represents andesite samples with 75 mm diameter and Fig. 3(d)-3(i) represent samples with 63 mm diameter, before and after the moment of failure.

According to Fig. 3(a), 3(d), and 3(g), the dashed and solid lines representing the force-time graph and the temperature change-time graph, respectively also indicate a sudden drop at the moment of failure. Fig. 3(b), 3(e), and 3(h) shows the thermography image before the failure moment, whereas Fig. 3(c), 3(f) and 3(i) shows the thermography image after the failure moment. The color range is selected as a rainbow profile from the software where blue colors represent lower temperature. By considering the local decrease in the force measurement, a varying increase of temperature at the moment of failure is observed for andesite samples with different sizes. Fig. 3(h) and 3(i) represent a lower room temperature and therefore are displayed in dark blue color according to the selected color profile of the software. Since the experiments were performed at different time intervals during the day, the color observed in thermographic images vary between green-blue color before the failure, and yellow-red color at the failure moment. There is no heat treatment (heating or cooling) of specimens that have similar surface morphology and color.

Table 2 summarizes the overall results for 75 mm and 63 mm diameter of andesite samples. The radiation energy provided for different sample diameters is calculated based on Eqs. (1) and (2).

According to Table 2, the temperature increase at the moment of failure for andesite samples with 75 mm diameter were 5.84°C higher compared to the temperature readings taken from 63 mm diameter samples. In addition, it has been observed that the amount of radiation energy

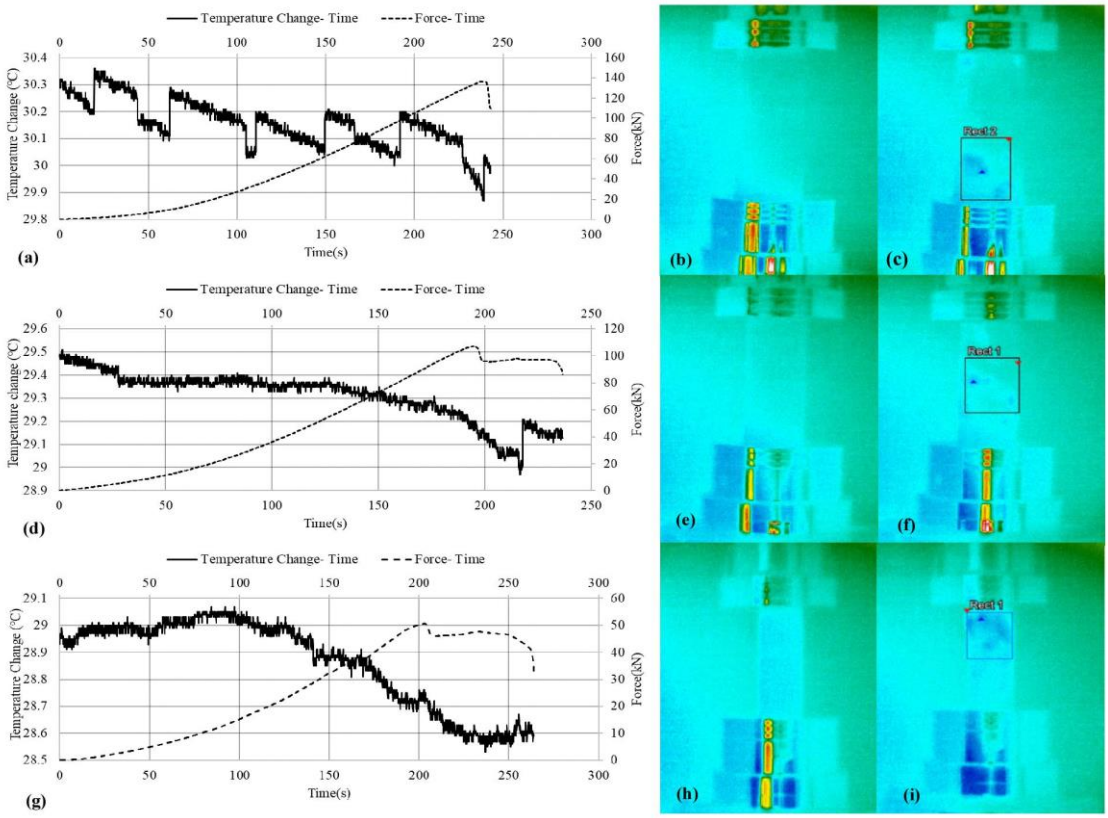

Fig. 4 (a), (d), (g) Temperature change - failure load - time graph of marble samples, (b), (e), (h) Thermography image of marble samples before failure and (c), (f), (i) Thermography image of marble samples after failure

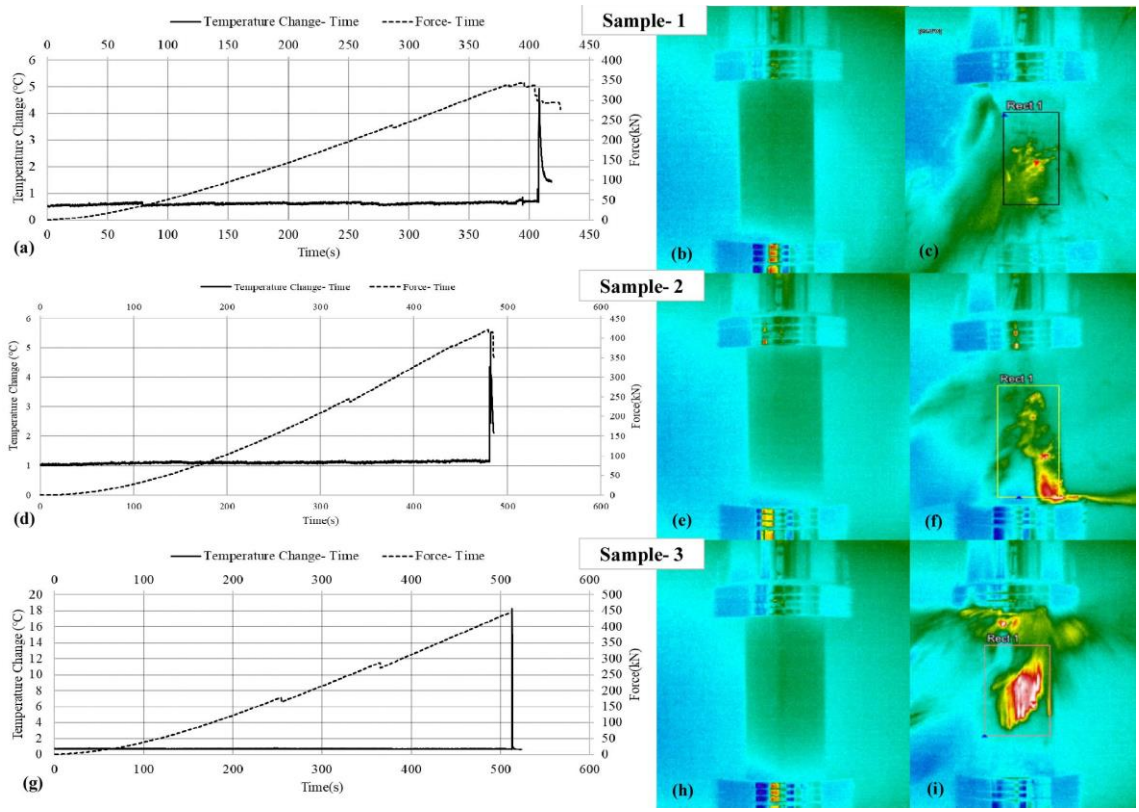

Fig. 5 (a,) (d), (g) Temperature change - failure load - time graph of gneiss-schist samples, (b), (e), (h) Thermography image of gneiss-schist samples before failure and (c), (f), (i) Thermography image of gneiss-schist samples after failure

Table 3 Average results for different sizes of marble samples

Sample Diameter (mm)	Failure Load (kN)	Temperature Decrease (°C)	Radiation Energy (kJ)
75	293.90	-	-
63	153.80	0.50	17.72
53	94.80	0.58	18.29
42	46.20	0.49	12.68
Average	147.20	0.53	16.23

Table 4 The overall results of the gneiss-schist samples

Sample	Failure Load (kN)	Temperature Increase (°C)	Radiation Energy (kJ)
Sample-1	345.80	4.94	91.81
Sample-2	419.31	5.51	192.21
Sample-3	443.69	18.27	288.36
Average	402.93	9.58	190.79

was 160 kJ higher than the amount of the radiation energy of 63 mm diameter samples. Hence, it can be said that there is a strong correlation between the increase in failure load and temperature increase.

Similar to the andesite samples, marble samples with 75 mm, 63 mm, 53 mm, and 42 mm diameter were prepared for UCS tests performed at the predetermined displacement rate of 0.002 mm/s. The experimental results of 63 mm, 53 mm, and 42 mm marble samples are given in Fig. 4(a), 4(d) and 4(g), respectively.

On the contrary to the behavior of the andesite samples, the temperature monitored on the surface of marble specimens decreased during the test period. According to Mineo & Pappalardo (2006), some rocks samples can show cooling behavior during experiments. The temperature decrease trend could not be observed for samples with 75 mm diameter for this study. Fig. 4 indicates the temperature decrease during some of the experiments for each diameter together with the thermography images of these samples before and after the failure moments, respectively. Dark blue regions in Fig. 4 reveals the colder regions on the sample and light blue regions were observed at the beginning of the experiments. Towards the end of the experiments, these light blue regions started to turn into darker blue regions based on the thermal camera recording. Therefore, it can be concluded that marble samples showed cooling behavior during the experiments. Some marble samples showed a scattered temperature change during the experiments. This was a phenomenon taken into account and it was considered that a combination of an acoustic emission system and a thermal camera could be used to obtain a more accurate relationship for such cases.

As it can be seen from Fig. 4(a), 4(d) and 4(g), the temperature decreased constantly during the experiments conducted on marble samples where the dark blue colors on the thermographic images represent the lower temperature values. Fig. 4(b), 4(e) and 4(h) represent the thermography image of marble samples before the failure moment, whereas Fig. 4(c), 4(f) and 4(i) are the thermography image of the marble samples after the failure moments. The temperature decrease recorded for marble samples is on a considerably low level resulting in a temperature change graph with fluctuations. Table 3 summarizes the average results for different sizes of all marble samples tested.

According to the experiment results summarized in Table 3, it was observed that the temperature decrease remained approximately constant at about 0.5-0.6°C regardless of the diameter of the marble specimen. Similarly, the released radiation energy amount remained almost constant for marble samples with different diameters. Compared to the andesite samples, gneiss-schist samples also followed a trend of temperature increase at the failure moment and were used for a comparison of the test results with the andesite samples. Fig. 5 represents the three valid tests in which the temperature increase was observed at the failure plane. As it was the case for the andesite samples, tests where low temperature increase was observed at the failure moment were classified as part of the non-valid experiments but were also analyzed. Fig. 5(a), 5(d), and 5(g) show the force-time graph and the temperature change-time graph, which indicate a sudden drop at the moment of failure. The thermography image before the failure moment visualizes the temperature profile that is mainly dominated by the room temperature as seen in Fig. 5(b), 5(e), and 5(h). Similarly, Fig. 5(c), 5(f) and 5(i) correspond to the thermography image after the failure moment and describe how the sudden temperature change is observed at the failure plane and the outburst of the specimen.

The varying temperature increase at the moment of failure was recorded for gneiss-schist samples during the failure and the behavior of the samples describe the local decrease in the force measurement. Table 4 summarizes the overall results for gneiss-schist samples.

As it can be seen from Table 4, released radiation energy and temperature at the failure plane increased in accordance with the failure load. As a result, it was observed that average failure load, temperature increase, and radiation energy were 402.93 kN, 9.57°C, and 190.79 kJ on average. Fig. 6 shows the correspondence between failure plane and temperature increase for andesite sample and the microscopic image of the failure plane where high temperature increase could be observed.

The failure plane observed on the photograph can be detected distinctly on the thermographic image as the location of the major cracks formed on the specimen are corresponding to the higher temperature changes. The reason of the energy dissipation from the specimens was considered as being related to the dislocation of grains on the failure plane. According to Fig. 6, vesicle development at some regions were detected under microscope. These vesicles arise from the dislocation of the grains around these regions. Hence, dislocation of the grains and the formation of the vesicles causes more radiation energy release from the specimen. For andesite and gneiss-schist samples with high temperature increase, correlation between the angle of failure plane and temperature increase at the failure moment was also investigated.

Figs. 7 and 8 represent the relationship between the angle of failure plane and the temperature increase at the failure moment of andesite samples and gneiss-schist

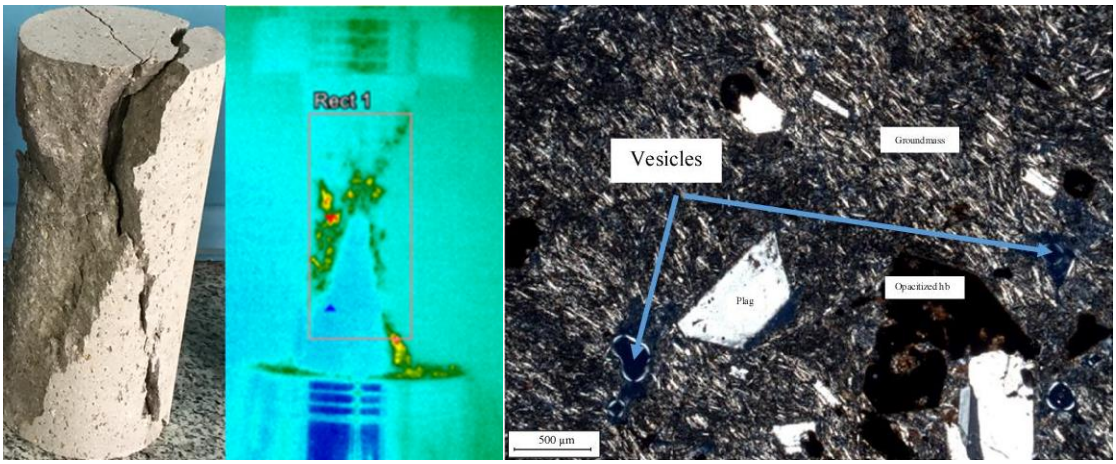

Fig. 6 Photograph and microscopic image of the andesite sample's failure plane

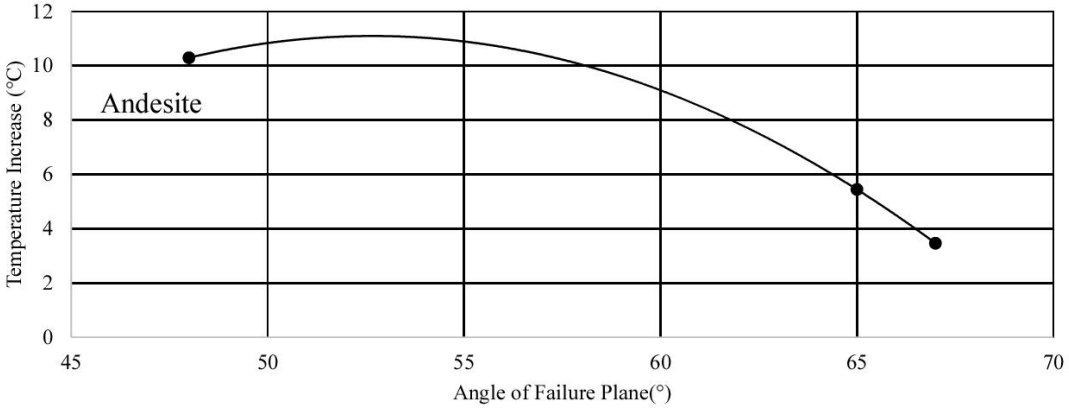

Fig. 7 Angle of failure plane - temperature increase graph of andesite samples

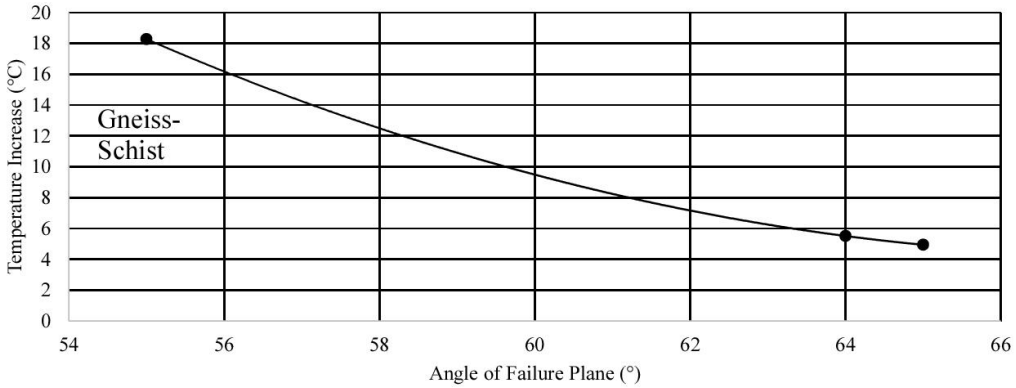

Fig. 8 Angle of failure plane - temperature increase graph of gneiss-schist samples

samples, respectively.

According to Fig. 7 and 8, lower temperature increase was recorded at the failure moment for andesite and gneiss-schist samples with increasing failure plane angle. This was interpreted as the lower failure plane angle causing more contact area between the grains and therefore, this results in higher temperature increase at the failure moment of the specimens due to the possibility of a longer period of friction. As also stated in various studies in the literature, this behavior represents brittle rock behavior. Hence, it is seen that brittle rocks are characterized by higher temperature increase at the failure moment. It is known that the temperature change and energy release occur through the pores of the material. Porosity rates of the samples prepared by coring from rock blocks were compared and the relationship between the porosity and released energy was also investigated. In this context, porosity ratios of andesite and marble samples were measured. The effective porosity and total porosity rates of the andesite samples were calculated as 5.65% and 20.97%, respectively. The effective and total porosity rates of the marble samples were found as 0.59% and 10.79%, respectively. The radiation energy values of the andesite and marble samples were calculated as 191.81 kJ and 16.23 kJ. Hence, it can be said

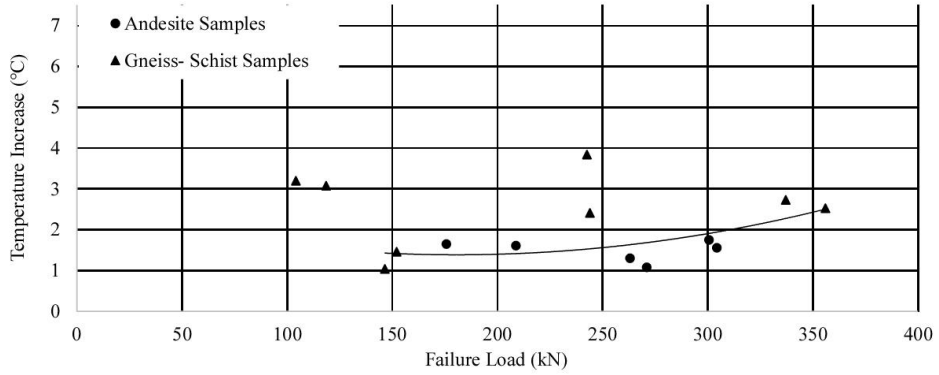

Fig. 9 Temperature increase-failure load graph of andesite and gneiss- schist samples with low temperature increase

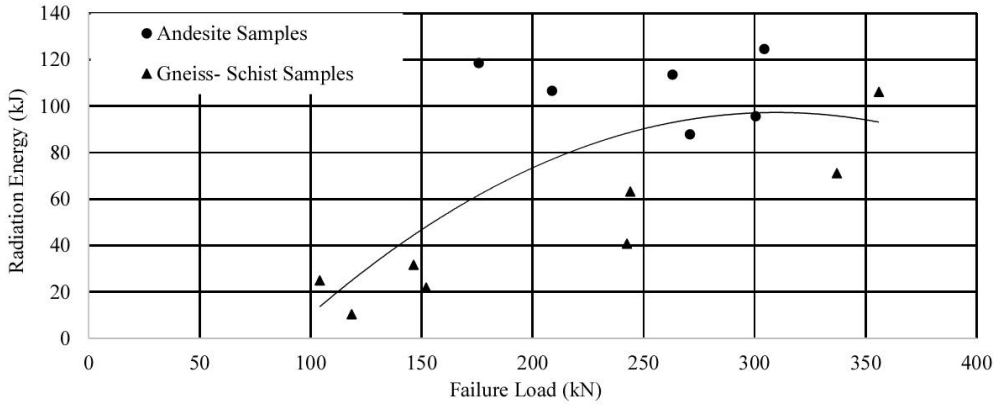

Fig. 10 Radiation energy-failure load graph of andesite and gneiss- schist samples with low temperature increase

that higher porosity of samples is related with a greater amount of released energy.

The amount of the temperature recorded for andesite and gneiss- schist samples according to failure load values for each sample can be illustrated individually as seen in Fig. 9.

According to Fig. 9, andesite samples follow the estimated trend line, whereas gneiss-schist samples showed more scattered behavior. Hence, for the samples with low temperature increase at the failure plane, an interpretation of the individual results could be misleading. Therefore, Fig.10 represents the amount of radiation energy released and failure load of andesite and gneiss-schist samples.

According to Fig. 10, the samples with a low temperature profile also do not follow a distinctive trend and it can be stated that the released energy amount increase with increasing failure load values.

4. Discussions

The experiments performed within the scope of the study were analyzed for different rock types, and since the core diameter of gneiss-schist samples was 63 mm, all samples were selected to have the same diameter for comparison purposes. Table 5 summarizes the complete test results of low and high temperature change observed andesite, gneiss-schist, and marble samples with 63 mm diameter. According to Table 5, it was observed that the

Table 5 Complete test results of 63 mm diameter samples at the failure plane

	Rock Type	UCS (MPa)	Temperature Change (°C)	Radiation Energy (kJ)
High Temperature Increase Samples	Andesite	79.10	4.45	139.21
	Gneiss - Schist	99.10	9.58	190.79
Low Temperature Increase Samples	Andesite	79.10	1.49	107.81
	Gneiss - Schist	99.10	2.54	46.27
	Marble	48.05	-0.50	17.72

increase in the measured strength results is similar to the average temperature increase at the failure moment for all specimens excluding marble. There was also an increase in the amount of radiation energy emitted for high temperature increase samples.

The increase in the measured UCS values is proportional to the increase in the temperature at the time of failure. According to the results of the andesite and gneiss-schist samples with low temperature increase at the failure moment, it was seen that the increase in the strength results defined a similar trend in the temperature increase at the failure moment. On the contrary, there was a decrease in the amount of radiation energy emitted with increasing strength. The main reason for this is explained by the effect of the structural differences, such as the grain structures of

different rock types on the failure behavior (Salami *et al.* 2017). As a result, it is concluded that the increase in the UCS values is proportional to the increase in the temperature at the time of failure for andesite and gneiss-schist samples.

The samples with low temperature increase at the failure plane indicate that there is a relationship between the failure load, the temperature increase at failure moment, and the released energy amounts. Although the thermal camera used during the experiments was not a high-speed device, the test results could be considered as representing the thermographic behavior of the rock specimens. The results can be considered as preliminary and indicated that the increase of failure load is observed similarly in both the temperature and the amount of energy released.

5. Conclusions

In this study, the failure behavior of different types of rock samples as a result of UCS tests was investigated with the help of thermographic analysis. The failure behavior of same type of rocks was investigated by varying specimen diameters. Main findings of the study can be summarized as follows;

• For andesite type rock samples, it was observed that for comparably larger diameter, the failure load varying between 283.3 kN to 437.6 kN could be related to the increase of the measured temperature from 4.45℃ to 10.29℃ at the failure plane and the increase of the generated energy from 139.21 kJ to 297.18 kJ.

• Similarly, for gneiss-schist type rock samples, the expected behavior of the temperature of the failure plane increasing in accordance to failure load was observed. The temperature at the failure plane increased from 4.94℃ to 18.27℃ with an increase in the failure load from 345.8 kN to 443.69 kN. Besides, the amount of energy released was found as increasing from 91.81 kJ to 288.36 kJ with greater amount of applied load.

• By considering the andesite and gneiss-schist type samples, respectively, there is a directly proportional relationship between the failure load and the amount of temperature recorded during the failure moment and released energy from the sample.

• For the different types of rock samples, the temperature increase monitored on the failure plane and released energy from the sample is higher for the samples with higher UCS values. For the andesite samples, the UCS value, the temperature increase, and the energy released were 79.10 MPa, 4.45 ℃ and 139.21 kJ whereas for gneiss-schist type samples these values were 99.10 MPa, 9.58℃ and 190.79 kJ, respectively. Therefore, it can also be concluded that the directly proportional relationship between the UCS, the amount of temperature generated during the failure moment, and released energy from the sample is valid for different types of rock samples used in the experiments.

• According to the structure of the rock, a temperature decrease can be seen instead of a temperature increase in some rock types. For marble samples, it was found that the temperature decrease value remained constant between 0.5℃ and 0.6℃ regardless of the diameter of the sample. However, it was observed that the amount of released energy was increased from 12.68 kJ to 18.29 kJ with the increase in the failure load.

In this study, the recorded temperature increase at the moment of failure, and the amount of radiation energy for different type of rock samples was aimed to be determined. Most of the studies in the literature about this research topic investigate the temperature profile at the failure moment by using mid-wave and high-speed thermal cameras. A longwave length thermal camera was used to investigate the temperature increase at the failure plane for different types of rock samples. In this context, longwave thermal cameras can provide preliminary results and the failure behavior of rocks could be investigated in more detail by supporting these results with other available technologies such as acoustic emission, digital image correlation (DIC), and high-speed thermal cameras. The failure plane of the specimens could be detected at only one surface of the specimen due to experimental setup with a single thermal camera. Recording other surfaces of the specimen with the help of multiple thermal cameras might be a future study to overcome some issues during experiments. In addition to these suggestions, the emissivity of different type of rock specimens can be investigated according to different surface morphology of samples. Similarly, rock samples can be pre-heated to elevated temperatures. This will provide a wider temperature range recorded by the thermal camera. Therefore, temperature change at the failure moment might be observed more distinctly. In this study, loading rate was kept constant. For future studies, different loading rates and cyclic loading will be used to analyze the effect of the loading rate on the specimens.

Acknowledgments

The research described in this paper was financially supported by the Middle East Technical University, Scientific Research Project GAP-305-2018-2724.

References

Abuel-Naga, H.M., Bouazza, A. and Gates, W. (2013), "Impact of bentonite form on the thermal evolution of the hydraulic conductivity of geosynthetic clay liners", *Géotechnique Lett*., **3**(2), 26-30. https://doi.org/10.1680/geolett.13.007.

Antony, S.J., Olugbenga, A., Ozerkan, N., Marumoame, O. and Okeke, G. (2017), "Sensing temperature and stress distributions on rock samples under mechanical", *Proceedings of the 15th Biennial ASCE Conference on Engineering, Science, Construction, and Operations in Challenging Environments*, Orlando, Florida, U.S.A., April.

Aydan, Ö. and Ulusay, R. (2013), "Geomechanical evaluation of derinkuyu antique underground city and its implications in geoengineering", *Rock Mech. Rock Eng*., **46**(4), 731-754. https://doi.org/10.1007/s00603-012-0301-7

Aydan, Ö., Manav, H., Yaoita, T. and Yagi, M. (2014), "Multi-parameter thermo-dynamic response of minerals and rocks during deformation and fracturing", *Proceedings of the ISRM International Symposium - 8th Asian Rock Mechanics Symposium*, Japan, Sapporo, October.

Cermak, V. and Rybach, L. (1982), *Thermal Conductivity and Specific Heat of Minerals and Rocks*, in *Geophysics- Physical Properties of Rocks*, Springer, 305-343.

Chen, G., Li, T., Wang, W., Guo, F. and Yin, H. (2017), "Characterization of the brittleness of hard rock at different temperatures using uniaxial compression tests", *Geomech. Eng.*, **13**(1), 63-77. https://doi.org/10.12989/gae.2017.13.1.063

Deb, D. and Verma, A.K. (2016), *Fundamentals and Applications of Rock Mechanics*, PHI Learning, New Delhi, India.

Go, G.H., Lee, S.R., Kim, Y.S., Park, H.K. and Yoon, S. (2014), "A new thermal conductivity estimation model for weathered granite soils in Korea", *Geomech. Eng.*, **6**(4), 359-376. http://doi.org/10.12989/gae.2014.6.4.359.

Gui, Y.L., Zhao, Z.Y., Ji, J., Wang, X.M., Zhou, K.P. and Ma, S.Q. (2016), "The grain effect of intact rock modelling using discrete element method with Voroni grains", *Géotechnique Lett.*, **6**(2), 136-143. https://doi.org/10.1680/jgele.16.00005.

He, M., Sousa, R., Miranda, T. and Zhu, G. (2015), "Rockburst laboratory tests database- Application of data mining techniques", *Eng. Geol.*, **185**, 116-130. https://doi.org/10.1016/j.enggeo.2014.12.008.

Hong-lin, M. (2013), "Rock mechanical behaviors testing by digital speckle correlation method", *J. Appl. Optics*, **34**, 123-127.

Jin, G.C., Wu, Z., Bao, N.K. and Yao, X.F. (2003), "Digital speckle correlation method with compensation technique for strain field measurements", *Opt. Lasers Eng.*, **39**, 457-464. https://doi.org/10.1016/S0143-8166(02)00028-3.

Kong, B., Wang, E. and Li, Z. (2018), "Regularity and coupling correlation between acoustic emission and electromagnetic radiation during rock heating process", *Geomech. Eng.*, **15**(5), 1125-1133. https://doi.org/10.12989/gae.2018.15.5.1125.

Lee, S.J., Kim, K.Y., Choi, J.C. and Kwon, T.H. (2016), "Experimental investigation on the variation of thermal conductivity of soils with effective stress, porosity, and water saturation", *Geomech. Eng.*, **11**(6), 771-785. http://doi.org/10.12989/gae.2016.11.6.771.

Lou, Q. and He, X. (2018), "Experimental study on infrared radiation temperature field of concrete under uniaxial compression", *Infrared Phys. Techn.*, **90**, 20-30. https://doi.org/10.1016/j.infrared.2018.01.033.

Ma, S., Wang, L. and Jin, G. (2006), "Damage evolution inspection of rock using digital speckle correlation method (DSCM)", *Key Eng. Mater.*, **326**, 1117-1120. https://doi.org/10.4028/www.scientific.net/KEM.326-328.1117.

Ma, S.P., Xu, X.H. and Zhao, Y.H. (2004), "The Geo-DSCM system and its application to the deformation", *Int. J. Rock Mech. Min. Sci.*, **41**, 292-297. https://doi.org/10.1016/j.ijrmms.2004.03.056.

Pappalardo, G., Mineo, S., Zampelli, S.P., Cubito, A. and Calcaterra, D. (2016), "Infrared thermography proposed for the estimation of the cooling rate index in the remote survey of rock masses", *Int. J. Rock Mech. Min. Sci.*, **83**, 182-196. https://doi.org/10.1016/j.ijrmms.2016.01.010.

Pasten, C., Garcia, M. and Carlos Santamarina, J. (2015), "Thermo-mechanical ratcheting in jointed rock masses", *Géotechnique Lett.*, **5**(2), 86-90. https://doi.org/10.1680/geolett.14.00118.

Read, R.S. (2004), "20 years of excavation response studies at AECL's underground research laboratory", *Int. J. Rock Mech. Min. Sci.*, **41**(8), 1251-1275. https://doi.org/10.1016/j.ijrmms.2004.09.012.

Salami, Y., Dana, C. and Hicher, P.Y. (2017), "Infrared thermography of rock fracture", *Géotech. Lett.*, **7**(1), 1-5. https://doi.org/10.1680/jgele.16.00131.

Tan, Y.Z., Liu, Y.X., Wang, P.Y. and Zhang, Y. (2016), "A predicting model for thermal conductivity of high permeability-high strength concrete materials", *Geomech. Eng.*, **10**(1), 46-57. https://doi.org/10.12989/gae.2016.10.1.049.

Tan, Z.H., Tang, C.A. and Zhu, W. (2007), "Infrared thermal image study on failure of granite with hole", *Key Eng. Mater.*, **353**, 2313-2316. https://doi.org/10.4028/www.scientific.net/KEM.353-358.2313.

Ulusay, R., Aydan, Ö., Gerçek, H., Hindistan, M.A. and Tuncay, E. (2016), *Rock Mechanics and Rock Engineering: From the Past to the Future*, CRC Press, London, U.K.

Vollmer, M. and Möllmann, K.P. (2017), *Infrared Thermal Imaging: Fundamentals, Research and Applications*, John Wiley & Sons, Weinheim, Germany.

Wang, C., Lu, Z., Liu, L., Chuai, X. and Lu, H. (2016), "Predicting points of the infrared precursor for limestone failure under uniaxial compression", *Int. J. Rock Mech. Min. Sci.*, **88**(10), 34-43. https://doi.org/10.1016/j.ijrmms.2016.07.004.

Wu, L., Liu, S., Wu, Y. and Wang, C. (2006), "Precursors for rock fracturing and failure—Part I: IRR image abnormalities", *Int. J. Rock Mech. Min. Sci.*, **43**(3), 473-482. https://doi.org/10.1016/j.ijrmms.2005.09.002.

Xie, H., Li, L., Peng, R. and Ju, Y. (2009), "Energy analysis and criteria for structural failure of rocks", *J. Rock Mech. Geotech. Eng.*, **1**(1), 11-20. https://doi.org/10.3724/SP.J.1235.2009.00011.

Yin, T., Li, X., Cao, W. and Xia, K. (2015), "Effects of thermal treatment on tensile strength of Laurentian granite using Brazilian test", *Rock Mech. Rock Eng.*, **48**(6), 2213-2223. https://doi.org/10.1007/s00603-015-0712-3.

Yin, T., Zhang, S., Li, X. and Bai, L. (2018), "Evolution of dynamic mechanical properties of heated granite subjected to rapid cooling", *Geomech. Eng.*, **16**(5), 483-493. https://doi.org/10.12989/gae.2018.16.5.483.

Young, R.P. and Collins, D.S. (2001), "Seismic studies of rock fracture at the underground research laboratory, Canada", *Int. J. Rock Mech. Min. Sci.*, **38**(6), 787-799. https://doi.org/10.1016/S1365-1609(01)00043-0.

Zhang, Q.B. and Zhao, J. (2014), "A review of dynamic experimental techniques and mechanical behaviour of rock materials", *Rock Mech. Rock Eng.*, **47**(4), 1411-1478. https://doi.org/10.1007/s00603-013-0463-y.

GC